Available online at www.sciencedirect.com
ScienceDirect
Trans. Nonferrous Met. Soc. China 33(2023) 1144−1155
Transactions of Nonferrous Metals Society of China
www.tnmsc.cn

Effect of strain rate on mechanical properties of HCP/FCC dual-phase $CoCrFeNiNb_{0.5}$ high-entropy alloy

Zi-hao MA[1], Bing HOU[1], Dong-yang QIN[1], Yu-long LI[2]

1. School of Aeronautics, Northwestern Polytechnical University, Xi'an 710072, China;
2. School of Civil Aviation, Northwestern Polytechnical University, Xi'an 710072, China

Received 25 August 2022; accepted 1 December 2022

Abstract: By using split-Hopkinson pressure bar, scanning electron microscope and transmission electron microscope, the influence of strain rate on mechanical behavior of the as-cast $CoCrFeNiNb_{0.5}$ high-entropy alloy (HEA) consisting of hexagonal close-packed (HCP) pro-eutectic phase and eutectic structure (HCP laminate and face-centered cubic (FCC) laminate) was investigated. As the strain rate increases from 1×10^{-4} to 6×10^{3} s^{-1}, it is found that yield strength does not increase evidently and that fracture strain drops drastically. Quasi-static deformation mechanism of HCP laminate is the multiplication of tangled dislocation. However, the dynamic deformation mechanism of HCP laminate is shearing. Shearing may lead to the formation of the micro-crack at low compression strain of 0.1. Since the number of the micro-crack increases rapidly with the increase of dynamic compression strain, the avalanche fracture of HEA, which is caused by the covalence of micro-crack evolved from the shearing of HCP laminate, occurred, contributing to the dynamic compressive embrittlement.

Key words: high-entropy alloy; eutectic structure; high strain rate; shearing; ductile-to-brittle transformation

1 Introduction

Owing to high entropy, sluggish diffusion, lattice distortion and cocktail effects, high entropy alloys (HEAs) exhibit several unique mechanical properties, such as ultra-high strength, super-plasticity, remarkably high fracture toughness and prominent wear resistance, and have attracted the increasing attention of material scientists [1−5]. As a kind of structural materials with tremendous application potential, the combination of strength and ductility for HEAs with face-centered cubic (FCC), body-centered cubic (BCC) and hexagonal close-packed (HCP) has been extensively investigated [6]. A great number of studies suggested that the strength and the plasticity of HEAs are strongly affected by the crystal structures and are mutually exclusive during quasi-static deformation [7−10]. It is reported that HEAs with cubic structure possess a low yield strength and high plasticity, while the HEAs with HCP structure have a high strength and low plasticity [8,11−15].

During the high-strain-rate deformation, the constituent phase of HEAs tends to demonstrate special deformation behavior that is hardly activated in quasi-static straining, such as FCC to HCP, FCC to BCC and reverse martensite to austenite transformation [3,5]. As a result, the trade-off between the strength and the plasticity of some HEAs might disappear as the strain rate increases to the magnitude of 10^{3} s^{-1}. It is reported that although the yield strength and the flow strength increase with the strain rate, the high-strain-rate deformation could not deteriorate the dynamic plasticity of HEAs [16−18]. Surprisingly, the recent investigation

Corresponding author: Dong-yang QIN, Tel: +86-15291457041, E-mail: qindongyang19831205@126.com;
Yu-long LI, Tel: +86-29-88494859, E-mail: liyulong@nwpu.edu.cn
DOI: 10.1016/S1003-6326(23)66171-0

of CHEN et al [19] showed that dynamic yield strength and plasticity of $TiZrHfTa_{0.7}W_{0.3}$ HEA, which was composed of HCP matrix and BCC precipitation, were higher than quasi-static yield strength and plasticity of the alloy. Owing to the prominent compatibility between the dynamic strength and dynamic plasticity, HEAs are potential for fabricating the impact-resistant components, such as advanced armors.

Recently, research has been devoted to the effect of Nb content on microstructures and mechanical properties of $CoCrFeNiNb_x$ HEA, and a novel FCC/HCP dual-phase HEA with the chemical composition of $CoCrFeNiNb_{0.5}$ has been designed [20,21]. The as-cast $CoCrFeNiNb_{0.5}$ HEA exhibits high yield strength and outstanding ductility during the quasi-static deformation due to the coupling of the high-strength HCP phase and high-plasticity FCC phase [22−24]. However, little is known about the dynamic mechanical performance of $CoCrFeNiNb_{0.5}$ HEA. In this work, the dynamic compressive tests are conducted on the as-cast $CoCrFeNiNb_{0.5}$ HEA, in order to obtain the explicit results on dynamic mechanical properties and to explore the dynamic deformation mechanism.

2 Experimental

Particles of Co, Cr, Fe, Ni and Nb, with the purity of 99.95%, were used as raw materials of $CoCrFeNiNb_{0.5}$ HEA. The HEA ingot was melted in the vacuum arc melting furnace for four times to ensure the compositional homogeneity. The final mass of the hemisphere HEA ingot was 200 g. The compression specimen, with the dimension of d3 mm × 3 mm, was machined from ingot for quasi-static compression test and dynamic compression test.

Quasi-static compression test was carried out on Instron−5895 testing machine at the strain rate of $1\times10^{-4}\ s^{-1}$. In order to investigate the micro-structural evolution during the quasi-static deformation, the strain-limited compression test with the strain of 0.1 and the strain-limited compression test with the strain of 0.2 were conducted.

The dynamic compression test was performed on split-Hopkinson pressure bar (SHPB) at the strain rate of $6\times10^{3}\ s^{-1}$. Figure 1(a) shows the experimental set-up of the SHPB. The diameter of steel bar was 12.7 mm, and the Cu impulse shaper, with the dimension of 3 mm × 3 mm × 0.3 mm, was placed between the striker bar and the incident bar. The strain ($\varepsilon(t)$) and the stress ($\sigma(t)$) of the specimen were calculated by [25,26]

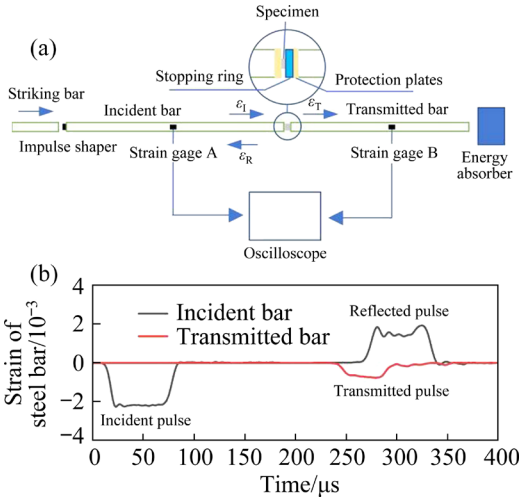

Fig. 1 Schematic illustration of split-Hopkinson pressure bar system (a), and typical loading waves in incident and transmitted bars (b)

$$\varepsilon(t)=-\frac{2C}{L_0}\int_0^T \varepsilon_R(t)\mathrm{d}t \tag{1}$$

$$\sigma(t)=E\frac{A}{A_0}\varepsilon_T(t) \tag{2}$$

where E is the elastic modulus of the incident steel bars, A and A_0 are the area of the specimen and the area of the transmitted bar, respectively, $\varepsilon_T(t)$ is the transmitted strain pulse, $\varepsilon_R(t)$ is the reflected strain pulse, C is the elastic wave velocity for the steel bar, and L_0 is the height of the compression specimen. The enlarged photograph of Fig. 1(a) demonstrates the optimized loading system of SHPB. Tungsten carbide (WC) plate were placed at the end of the incident bar and the transmitted bar to protect the loading surface. The specimen was placed between the WC plates. In order to investigate the microstructure evolution during the dynamic deformation, the strain-limited dynamic compression test was performed with the strain of 0.1 and 0.2 by using the stopping ring with the height of 2.7 and 2.4 mm. The strain limited specimen and the ruptured specimen were cut in half along the compression direction, mounted into resin and finally prepared into the metallographic specimens. Figure 1(b) shows the typical loading waves in incident and transmitted bars.

The constituent phase for the compression specimen of $CoCrFeNiNb_{0.5}$ HEA was identified by Bruker D8-Advance X-ray diffractometer (XRD). Co K_α source was used, and the scanning speed was 3 (°)/min. The microstructure of the HEA was investigated by using Zeiss-Stemi2000c optical microscope (OM) and Zeiss Supra-55 scanning electron microscope (SEM). Since the dimension of HEA compression specimen was *d*3 mm × 3 mm, it was hard to prepare the conventional *d*3 mm double-jet TEM specimen from the HEA specimen after the quasi-static compression test and the dynamic compression test. Therefore, FEI Helios 600 focused ion beam (FIB) SEM was used to machine the transmission election microscope (TEM) foils from the pro-eutectic HCP phase and the eutectic structure. FEI Themis Z probe-corrected TEM was used to observe the micro-structure of HEA in the bright field mode and the high angle annular dark field (HAADF) mode. Chemical compositions for the HCP phase and the FCC phase of the HEA were measured by energy dispersive spectrometer (EDS) equipped in the TEM.

3 Results

3.1 Microstructures and mechanical properties

Figure 2 shows the XRD pattern of the as-cast $CoCrFeNiNb_{0.5}$ HEA. The diffraction peaks are identified as HCP phase and FCC phase, which is in agreement with the XRD patterns reported in Ref. [16−18]. The XRD patterns indicate that the HEA consists of FCC phase and HCP phases.

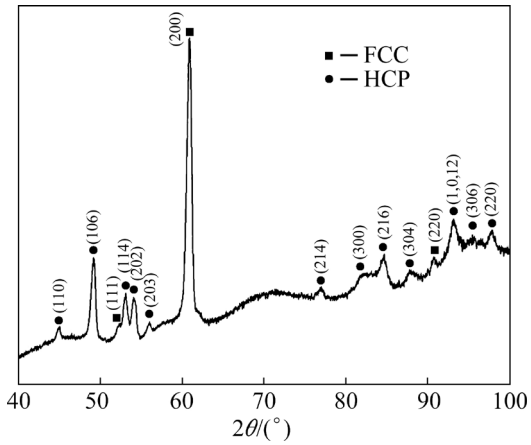

Fig. 2 XRD pattern of as-cast $CoCrFeNiNb_{0.5}$ HEA

Figure 3(a) presents the optical microscope image of $CoCrFeNiNb_{0.5}$ HEA. The HEA is composed of the snowflake-like pro-eutectic phase with the bright contrast and the equiaxial eutectic structure with the dark contrast. Figure 3(b) shows the SEM image of the $CoCrFeNiNb_{0.5}$ HEA, in which the pro-eutectic phase and equiaxial eutectic structure could also be observed. Figure 3(c) demonstrates the high magnification SEM image of pro-eutectic phase, while the detailed micro-

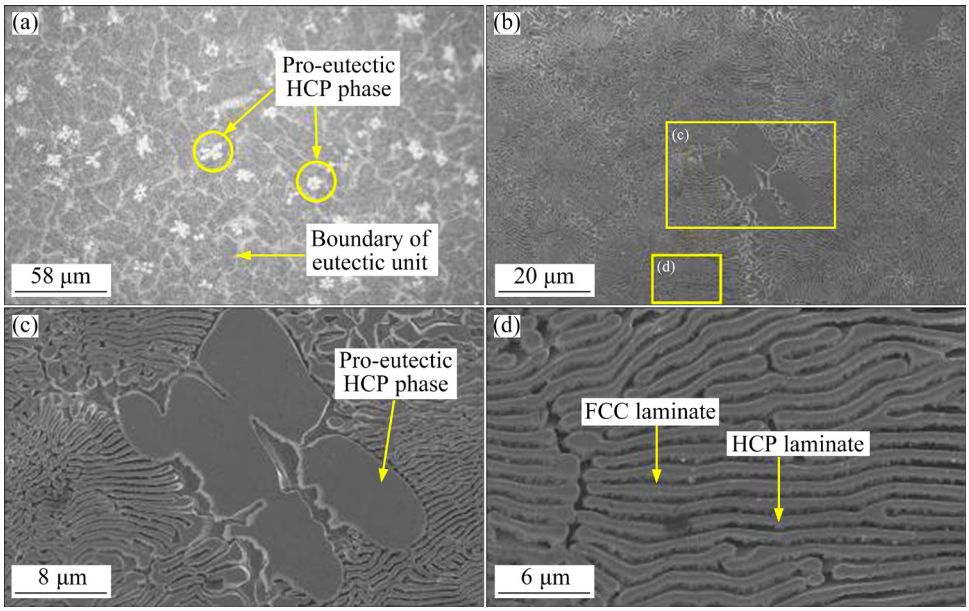

Fig. 3 Microstructures of as-cast $CoCrFeNiNb_{0.5}$ HEA: (a) Low-magnification optical microscope image; (b) Low-magnification SEM image; (c) High-magnification SEM image of pro-eutectic HCP phase shown in Fig. 3(b); (d) High-magnification SEM image of lamellar eutectic unit shown in Fig. 3(b)

structure for the eutectic unit is shown in Fig. 3(d). It is found that the thickness of the laminates is approximately 300 nm.

Figure 4(a) shows the bright-field TEM images of the as-cast $CoCrFeNiNb_{0.5}$ HEA, and the electron diffraction patterns of the dark laminate and the bright laminate are shown in Figs. 4(b) and 4(c), respectively. These diffraction patterns suggest that FCC laminate exhibits the bright contrast. In contrast, the HCP phase of the HEA, which exists as both pro-eutectic phase and laminate, exhibits the dark contrast in the bright-field TEM image. It can also be seen from Fig. 4(a) that the FCC phase only processes a few dislocations and that the HCP phase is almost dislocation-free. These findings indicate that the dislocation density of the as-cast HEA is considerably low.

Figure 5(a) shows the HAADF-TEM image of the as-cast HEA, and Figs. 5(b−f) display the corresponding EDS mappings of Co, Cr, Fe, Ni and Nb. It should be noted that the EDS mappings are recorded in the same position of Fig. 5(a). Table 1 gives the chemical compositions of the FCC phase and HCP phase. The FCC phase is enriched with Cr, Fe and Ni, while the HCP phase is enriched with Co and Nb.

Figure 6 shows the compressive stress−strain curves of the HEA. It is obvious that the mechanical properties of the alloy changes dramatically as the strain rate increases from 1×10^{-4} to 6×10^{3} s^{-1}. First, the yield strength of the alloy increases from 1726 to 2015 MPa. Then, the dynamic fracture strain is only 20.9%, which is only half of the quasi-static fracture strain of the HEA.

3.2 Deformation of $CoCrFeNiNb_{0.5}$ HEA in quasi-static compression

Figure 7(a) exhibits the low-magnification SEM image of the HEA specimen with the compression strain of 0.1. The compression direction is vertical. Compared with the initial microstructure of HEA (Fig. 3(b)), the morphology of the pro-eutectic HCP phase remains unchanged. However, it is observed that the aspect ratio of several eutectic structures increases. Figure 7(b) shows the high-magnification SEM image for the elongated eutectic structure. The HCP laminate and the FCC laminate are bent simultaneously in the boundary region of the eutectic structure. In the center of the eutectic structure, the normal direction of the HCP laminate and the FCC laminate tends to rotate towards the elongation direction. These findings indicate that in the initial quasi-static compression stage the plastic deformation of HEA concentrates in the center of the eutectic structures.

Figure 7(c) exhibits the SEM image of the HEA specimen with the compression strain of 0.2. With the increasing in the compressive strain, it is found that the aspect ratio for most of the eutectic structures increases evidently and that the grain boundary of the eutectic structure has been distorted.

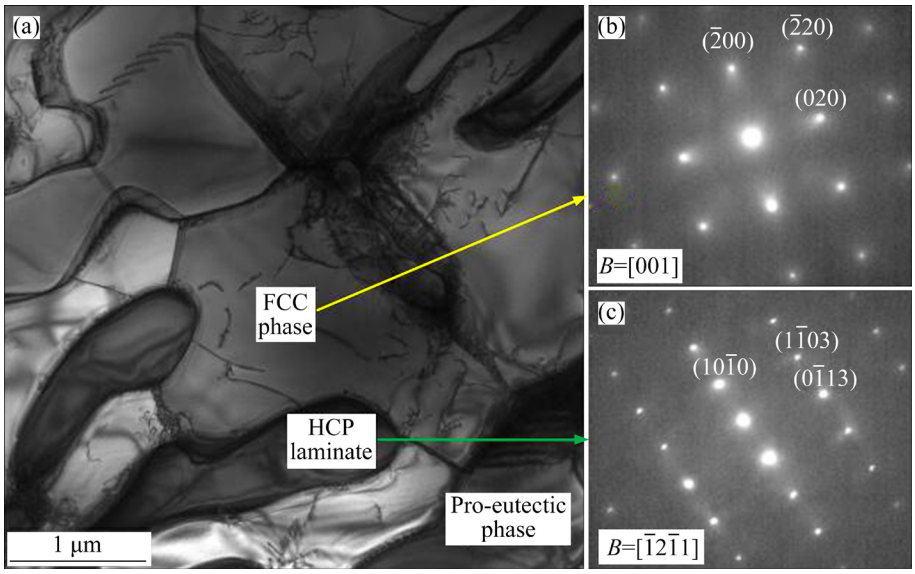

Fig. 4 TEM images of as-cast $CoCrFeNiNb_{0.5}$ HEA: (a) Bright-field TEM image; (b) Selected area electron diffraction pattern of FCC phase; (c) Selected area electron diffraction pattern of HCP phase

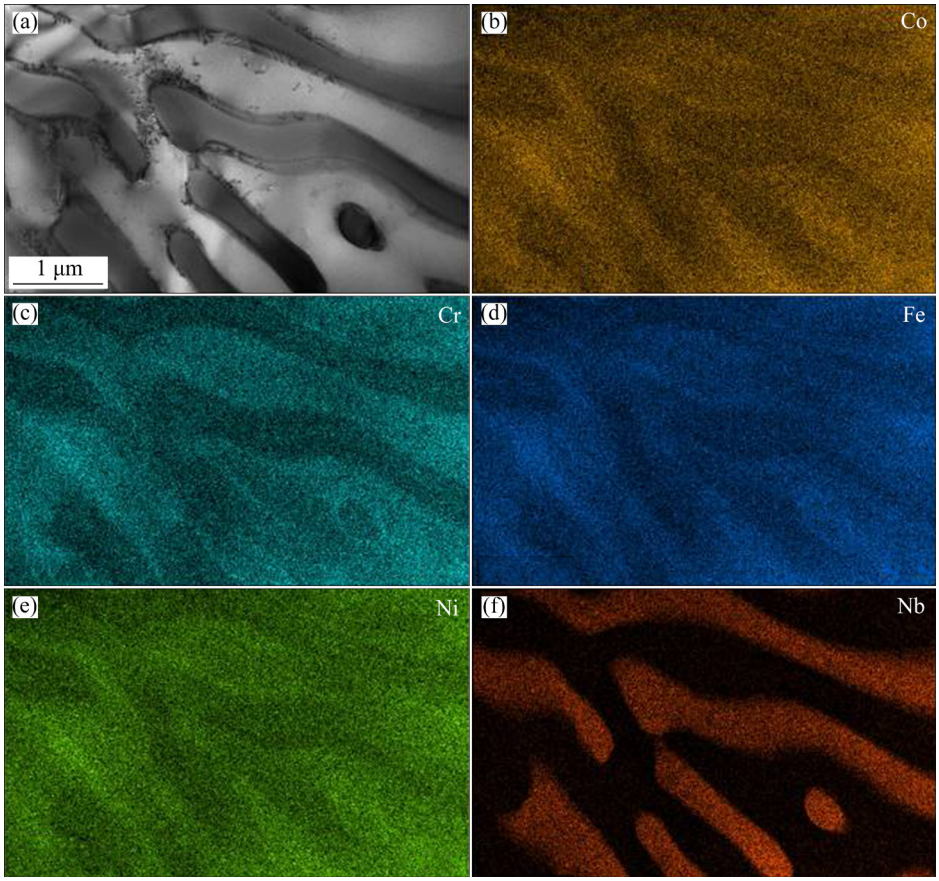

Fig. 5 Alloying element distributions in HCP phase and FCC phase of as-cast $CoCrFeNiNb_{0.5}$ HEA: (a) HAADF-TEM image; (b−f) EDS mappings for Co, Cr, Fe, Ni and Nb, respectively

Table 1 Chemical compositions for FCC phase and HCP phase of $CoCrFeNiNb_{0.5}$ HEA (at.%)

Phase	Co	Cr	Fe	Ni	Nb
FCC	20.5	27.7	25.1	23.7	3.0
HCP	23.9	16.8	20.0	19.1	20.2

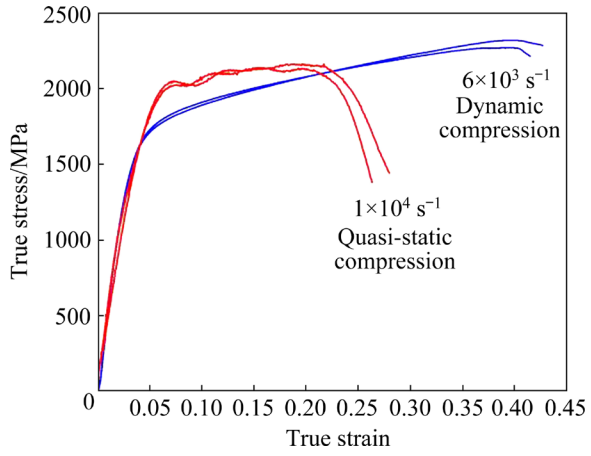

Fig. 6 Compressive stress−strain curves of as-cast $CoCrFeNiNb_{0.5}$ HEA (The strain rate of quasi-static compression test is 1×10^{-4} s^{-1}, while the strain rate of dynamic compression test is 6×10^{3} s^{-1})

However, the morphology of pro-eutectic HCP phase almost remains unchanged. These results suggest that the pro-eutectic phase of the HEA could act as the hard particle during the quasi-static deformation. Figure 7(d) shows the high-magnification SEM image recorded in the center of the dramatically-deformed eutectic unit. The normal direction of the HCP laminate and the normal direction of the FCC laminate also tend to rotate toward the same direction, which is the same as Fig. 7(b). Therefore, the eutectic structure of the HEA is capable of deforming severely during the quasi-static compression.

Figure 7(e) displays the SEM image recorded in the ruptured HEA specimen. Although the distortion of the eutectic structure becomes more dramatic, the pro-eutectic HCP phase, which is the hard particle of the $CoCrFeNiNb_{0.5}$ HEA, is still snowflake-like. Figure 7(f) shows the SEM image recorded in the region beneath the fracture surface of HEA. The shearing of the HCP laminate right beneath the fracture surface could be observed, and the original long HCP laminate has been sheared

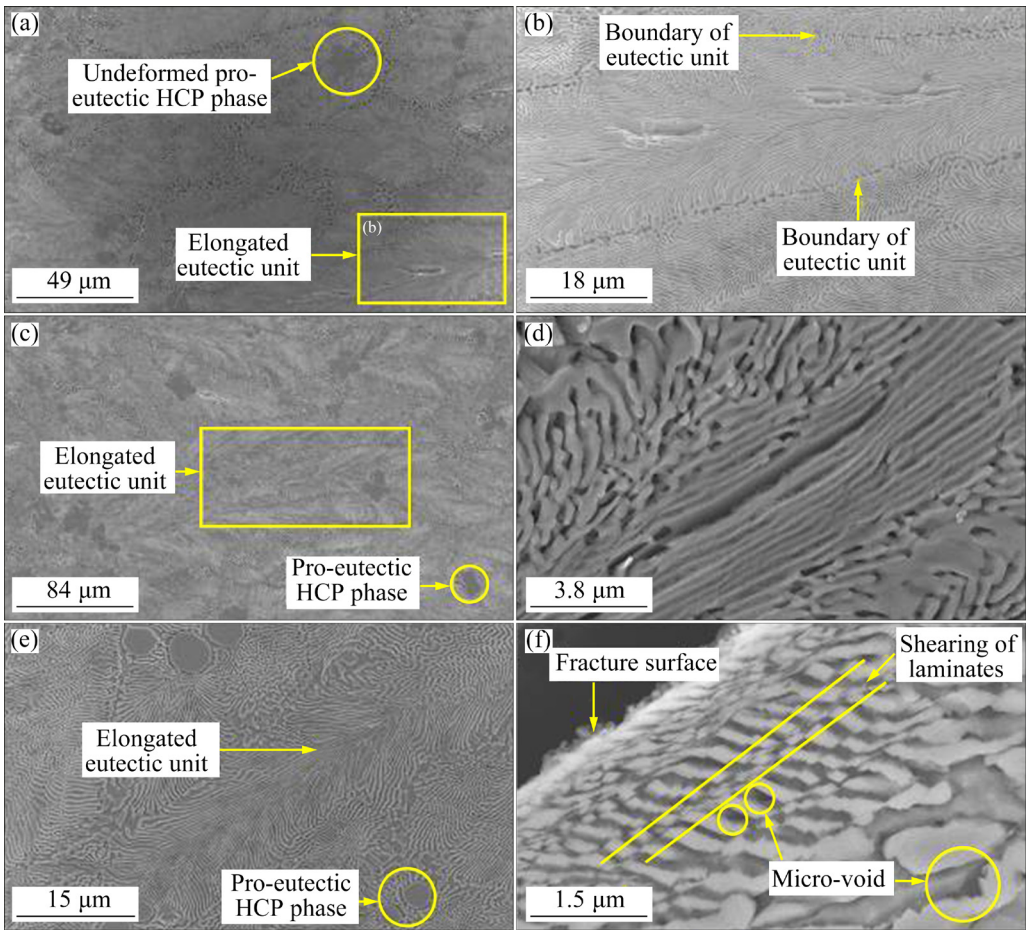

Fig. 7 Microstructural evolution of $CoCrFeNiNb_{0.5}$ HEA during quasi-static compression (The compressive strain rate is $1\times10^{-4}\ s^{-1}$, and the loading direction is vertical): (a) Low-magnification SEM image of HEA at compression strain of 0.1; (b) High-magnification SEM image of deformed eutectic unit with compression strain of 0.1; (c) Low-magnification SEM image of HEA at compression strain of 0.2; (d) High-magnification SEM image of deformed eutectic unit with compression strain of 0.2; (e) Low-magnification SEM image of ruptured HEA; (f) High-magnification SEM image recorded beneath compression fracture surface

into short sections. In the meantime, some micro-voids could be found on the interface between the HCP laminate and the FCC laminate. This suggests that the delamination of the HCP/FCC interface should be the damage mechanism of the HEA in quasi-static deformation, and that shearing fracture is the failure mechanism.

Figure 8 displays the TEM images of the ruptured specimen. It should be noted that the compression strain of the specimen is higher than 0.4. Figure 8(a) shows the TEM image of pro-eutectic HCP phase. As mentioned above, the quasi-static deformation of the HEA specimen could not bring in the obvious change in the morphology of the pro-eutectic HCP phase. Compared with the TEM image for pro-eutectic phase of the as-cast HEA (Fig. 4), a few micro-bands are observed within the pro-eutectic phase of the ruptured specimen. The micro-band is composed of numerous geometrically-necessary dislocations (GNDs) [27−29]. Furthermore, the dislocations could not be observed in the region outside the GNDs. The unaltered morphology and the low dislocation density of the pro-eutectic phase suggest that the plastic deformation of the hard pro-eutectic HCP phase is considerably limited during the quasi-static compression. Figure 8(b) shows the TEM image of the eutectic structure. The FCC laminate processes the bright contrast, while the HCP laminate exhibits the dark contrast. Compared with the TEM image for the eutectic structure of the as-cast HEA (Fig. 4), it can be found that the dislocation density of the FCC laminate and the HCP laminate considerably

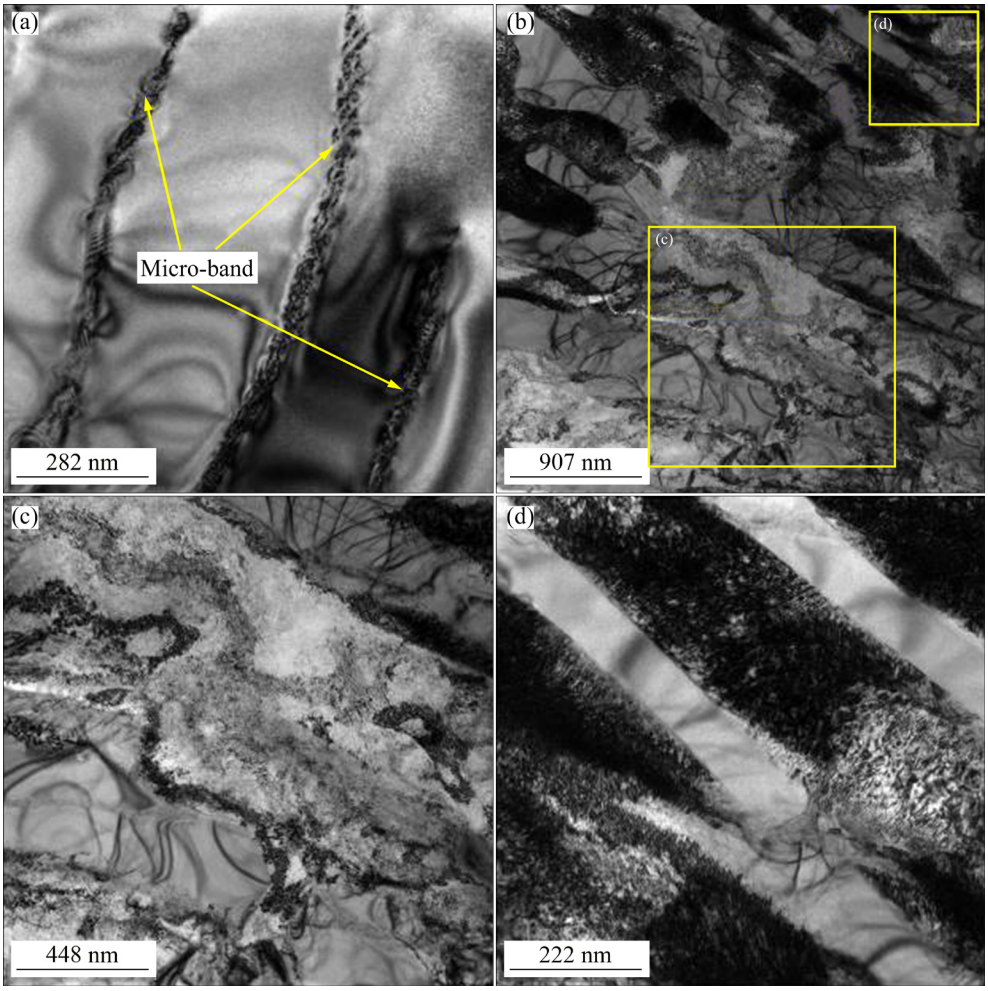

Fig. 8 TEM imgaes of ruptured $CoCrFeNiNb_{0.5}$ HEA (The compressive strain rate is 1×10^{-4} s^{-1}): (a) Pro-eutectic HCP phase; (b) Eutectic structure; (c) High-magnification TEM image of FCC phase in rectangular region of Fig. 8(b); (d) High-magnification TEM image of HCP laminate in rectangular region of Fig. 8(b)

increases. Figure 8(c) shows the high-magnification TEM image recorded in the rectangle region of Fig. 8(b). The deformed FCC phase has the structure of dislocation cells. Figure 8(d) shows the high-magnification TEM image recorded in the rectangle region of Fig. 8(b). The deformed HCP laminate has a tangled dislocation structure.

3.3 Microstructural evolution of $CoCrFeNiNb_{0.5}$ HEA during dynamic compression

Figure 9(a) shows the low-magnification SEM image of the HEA specimen with the dynamic compression strain of 0.1. The morphology of the pro-eutectic HCP phase remains unaltered, and the aspect ratio of partial eutectic structures increases considerably. In addition, the plastic deformation of the eutectic structure also concentrates in the center of the eutectic structure. Figure 9(b) shows the high-magnification SEM image of the deformed eutectic structure. Most of the HCP laminates and the FCC laminates are kinked. Furthermore, it is surprising that a small amount of micro-cracks, which are marked by the circles, could be observed within the HCP laminate. This indicates that the dynamic deformation of the HEA could bring in the damage of the HCP laminate at the low compression strain of 0.1. Figure 9(c) shows the SEM image of the deformed HEA specimen with the compression strain of 0.2. The morphology of pro-eutectic HCP phase remains unaltered. However, most of the eutectic structures start to deform as the compression strain increases to 0.2. Fig. 9(d) displays the SEM image recorded in the center of the elongated eutectic structure. Compared with Fig. 9(b), the numbers of the micro-crack within the HCP laminate increase evidently.

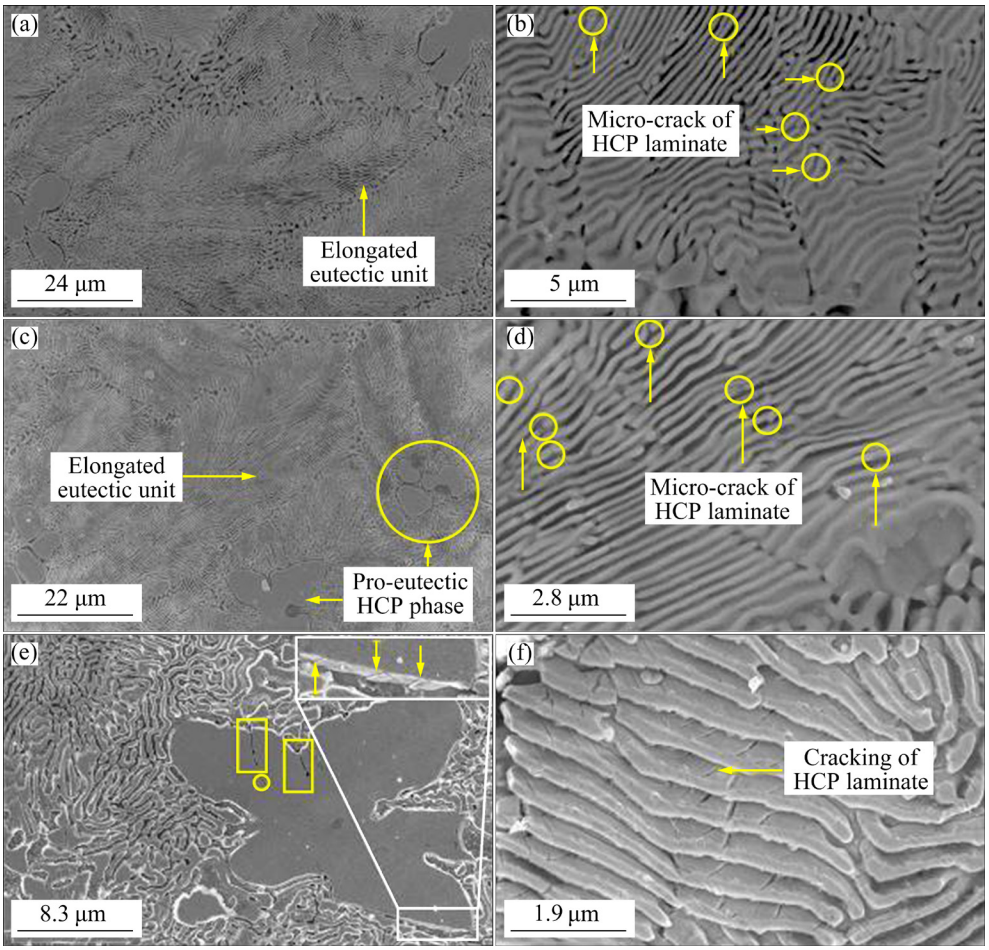

Fig. 9 Microstructural evolution of $CoCrFeNiNb_{0.5}$ HEA during dynamic compression (The loading direction is vertical, and the compression strain rate is 6×10^3 s^{-1}): (a) Low-magnification SEM image at compression strain of 0.1; (b) High-magnification SEM image of eutectic structure at compression strain of 0.1; (c) Low-magnification SEM image of HEA at compression strain of 0.2; (d) High-magnification SEM image of eutectic structure at compression strain of 0.2; (e) SEM image of pro-eutectic HCP phase of ruptured HEA; (f) SEM image of eutectic structure of ruptured HEA

Figure 9(e) illustrates the SEM image for pro-eutectic HCP phase of the ruptured HEA compression specimen. Although the morphology of pro-eutectic phase is still snowflake-like, the micro-crack within the pro-eutectic phase and the micro-crack in the boundary of pro-eutectic could be observed. The insertion of Fig. 9(e) shows the enlargement of the white rectangle region. The sharp steps, which are indexed by yellow allows, are present on the edge of the damaged pro-eutectic HCP phase. Figure 9(f) shows SEM image for the deformed eutectic structure. There are a large number of micro-cracks in each HCP laminate. Compared with the quasi-static compressive deformation, the dynamic compressive damage mechanism of HEA changes dramatically. It should be pointed out that the HEA specimen is shattered into pieces after the dynamic compression.

Figure 10(a) displays the TEM image of the pro-eutectic phase of the ruptured HEA. The micro-band composed of GDNs can be found, and the region outside the micro-band is still dislocation-free. This indicates that the deformation mechanism of the pro-eutectic phase is not affected by the strain rate. However, the micro-crack could be found within the micro-band of pro-eutectic phase, as shown in Fig. 10(b). Figure 10(c) shows the TEM image of the eutectic structure for the ruptured HEA. Except for the dislocation cells, the micro-band also appears in the deformed FCC laminate marked by the white squares. As mentioned in Fig. 8(d), the deformed HCP laminate of HEA is full of tangled dislocations after the quasi-static compression. However, compared with the quasi-static deformation behavior for HCP laminate, the dislocation structure of HCP laminate

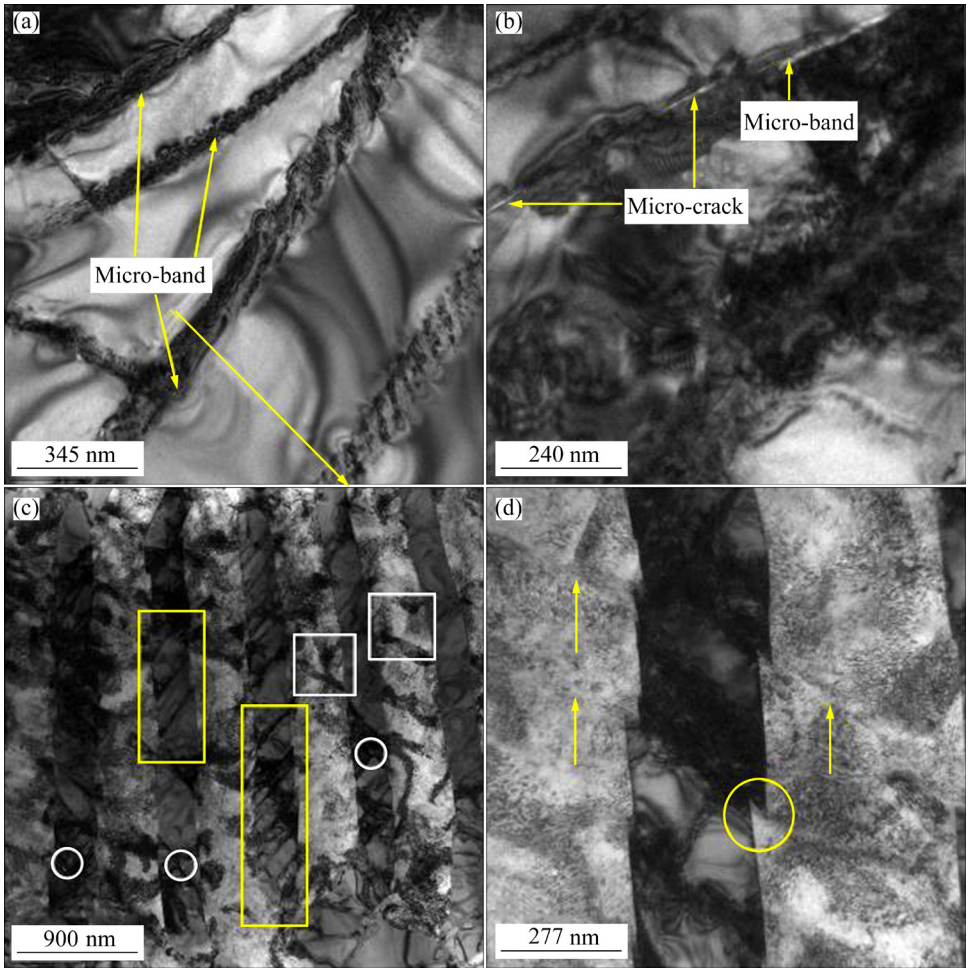

Fig. 10 TEM images for ruptured $CoCrFeNiNb_{0.5}$ HEA (The compressive strain rate is 6×10^3 s^{-1}): (a) Pro-eutectic HCP phase; (b) Micro-band of pro-eutectic HCP phase; (c) Eutectic structure; (d) Shearing deformation of HCP laminate

changes dramatically after dynamic compression. The deformation characteristic in HCP laminate is mainly shearing, and the shearing regions are marked by the yellow rectangles. Interestingly, nano-scaled cracks marked by the while circle could also been observed on the shearing plane. It is possible that the formation of the through-thickness micro-crack within the HCP laminate (Fig. 9(f)) might be caused by the propagation of the nano-scaled crack along the shearing plane. Figure 10(d) shows the TEM image of the deformed HCP laminate. As marked by the yellow circles, sharp edges could be found on the interface between the HCP laminate and the FCC laminate. The traces of the slipping plane for the neighboring FCC laminate are marked by the yellow arrows, suggesting that the FCC laminate might slip simultaneously to accommodate the shearing of the HCP laminate during the dynamic compression.

4 Discussion

4.1 Deformation mechanism of dynamic compression

The HCP laminate of the $CoCrFeNiNb_{0.5}$ HEA is the Fe_2Nb-type Laves phase and exhibits C14 crystal structure (Pearson symbol: $hP12$) [23]. Basal slip system including $(0001)\langle 11\bar{2}0\rangle$ and $(0001)\langle 1\bar{1}00\rangle$, prismatic slip system $\{1\bar{1}00\}\langle 11\bar{2}0\rangle$ and pyramidal slip system $\{10\bar{1}1\}\langle 10\bar{1}2\rangle$ are the main slip systems of C14-type Laves phase [30,31]. It is reported that the critical resolved shear stress (CRSS) values of the basal slip system and the non-basal slip system are comparable, and the slip system that has the greatest resolved shear stress is most likely to be activated [30]. Commonly, the slip mechanism of C14 type Laves phase was investigated by the compression of single-crystal micropillar [30−34]. For the small-sized Laves

micropillar with the fixed orientation to the applied load, only one slip system could be activated in compression, which leads to the shearing deformation and the fracture [30−34]. The shearing deformation of the HCP laminate, which is induced by the dynamic compression, is the same as the shearing of C14 type Laves micro-pillar. Therefore, it is possible that each HCP laminate, which is in the eutectic structure of the $CoCrFeNiNb_{0.5}$ HEA, might process only one slip system mentioned above during the high-strain-rate deformation, leading to the shearing deformation of the HCP laminate. Consequently, the shearing deformation of HCP laminate is due to the slip that is dominated by the single slip system during the dynamic compression.

For the pro-eutectic phase, the deformation characteristics are the micro-band and the crack within the micro-band, and shearing deformation also occurs. It is understandable that the shearing might lead to stress concentration in the boundary of pro-eutectic phase, which promotes the micro-crack initiation and propagation of the crack.

4.2 Dynamic compressive embrittlement

The HCP/FCC dual-phase $CoCrFeNiNb_{0.5}$ HEA exhibits embrittlement during the high-strain-rate compression. It is interesting that the compressive embrittlement of the HEA is not caused by the forming of the adiabatic shearing band at the low compression strain. However, microstructural analysis suggests that the dynamic compression embrittlement of the HEA is mainly caused by the embrittlement of the HCP laminate inside the eutectic structure. The quasi-static deformation of the HCP laminate is dominated by tangled dislocations, and the multiplication of dislocations does not lead to the damage of the HCP laminate. However, the dynamic deformation of the HCP laminate is dominated by the shearing deformation, and the micro-crack might start to form on the shearing plane as the compression strain reaches 0.1. In addition, the number of the micro-cracks increases continuously with the increase in dynamic compression strain. In the ruptured HEA, the density of the micro-cracks in each HCP laminate is so high that the distance between the cracks is less than 500 nm. Therefore, the high density of the cracks within the HCP laminate could lead to the avalanche failure of HEA at the low compression strain. It should be noted that the cracks of the pro-eutectic phase might also contribute to the dynamic compressive embrittlement of $CoCrFeNiNb_{0.5}$ HEA.

The compression embrittlement of the as-cast $CoCrFeNiNb_{0.5}$ HEA should be the disadvantage to the application of impact-resistant structures, because the micro-crack tends to form in the HCP laminate even though the structures are subjected to the low energy impact. In order to improve the damage resistance of the as-cast $CoCrFeNiNb_{0.5}$ HEA, it is suggested that the morphologies of the HCP laminate and the pro-eutectic HCP phase should be tailored [35−37]. First, thermal-mechanical processing should be conducted on the as-cast $CoCrFeNiNb_{0.5}$ HEA below the dynamic recrystallization temperature to break down the HCP laminate and the pro-eutectic HCP phase and to trigger the dynamic recrystallization of the FCC laminate. Second, the recrystallization annealing should be performed on the thermo-mechanically processed HEA. The recrystallization annealing might lead to the spheroidization of HCP phase, which is similar with morphology transformation of HCP laminate for titanium alloys [38,39].

5 Conclusions

(1) The $CoCrFeNiNb_{0.5}$ HEA consists of pro-eutectoid HCP phase and eutectic structure including FCC laminate and HCP laminate, and Co and Nb are enriched in the HCP phase.

(2) Compared with the pro-eutectoid HCP phase, the eutectic structure is the softer region of the HEA during the quasi-static compression and the dynamic compression.

(3) The shearing deformation of the HCP laminate could be activated during high-strain-rate deformation, contributing to dynamic compressive embrittlement of the HEA.

(4) The fracture of $CoCrFeNiNb_{0.5}$ HEA during the dynamic compression is mainly due to the covalence of the high-density micro-cracks within the brittle HCP laminate.

Acknowledgments

This work was supported by the National Natural Science Foundation of China (Nos. 11872317, 11972310), the Project of Key Laboratory of Impact and Safety Engineering

(Ningbo University), Ministry of Education, China (No. CJ202208) and Science Challenge Project, China (No. TZ2018001).

References

[1] GANGIREDDY S, GWALANIA B, LIU Kai-miao, BANERJEE R, MISHRA R S. Microstructures with extraordinary dynamic work hardening and strain rate sensitivity in $Al_{0.3}$CoCrFeNi high entropy alloy [J]. Materials Science and Engineering A, 2018, 734: 42−50.

[2] PAN Qing-song, ZHANG Ling-xue, FENG Rui, LU Qiu-hong, AN Ke, CHUANG A C, POPLAWSKY J D, LIAW P K, LU Lei. Gradient cell-structured high-entropy alloy with exceptional strength and ductility [J]. Science, 2021, 374: 984−989.

[3] LI Ze-zhou, ZHAO Shi-teng, RITCHIE R O, MEYERS M A. Mechanical properties of high-entropy alloys with emphasis on face-centered cubic alloys [J]. Progress in Materials Science, 2019, 102: 296−345.

[4] YE Y X, LIU C Z, Wang H, NIEH T G. Friction and wear behavior of a single-phase equiatomic TiZrHfNb high-entropy alloy studied using a nanoscratch technique [J]. Acta Materialia, 2018, 147: 78−89.

[5] FAN X J, QU R T, ZHANG Z F. Remarkably high fracture toughness of HfNbTaTiZr refractory high-entropy alloy [J]. Journal of Materials Science & Technology, 2022, 123: 70−77.

[6] GEORGE E P, CURTIN W A, TASAN C C. High entropy alloys: A focused review of mechanical properties and deformation mechanisms [J]. Acta Materialia, 2020, 188: 435−474.

[7] HU Meng-lei, SONG Wei-dong, DUAN Da-bo, WU Yuan. Dynamic behavior and microstructure characterization of TaNbHfZrTi high-entropy alloy at a wide range of strain rates and temperatures [J]. International Journal of Mechanical Sciences, 2020, 182: 105738.

[8] JIANG Kun, REN Teng-fei, SHAN Gui-bin, YE Tian, CHEN Lian-yang, WANG Cun-xian, ZHAO Feng, LI Jian-guo, SUO Tao. Dynamic mechanical responses of the $Al_{0.1}$CoCrFeNi high entropy alloy at cryogenic temperature [J]. Materials Science and Engineering A, 2020, 797: 140125.

[9] YE Y F, WANG Q, LU J, LIU C T, YANG Y. High-entropy alloy: Challenges and prospects [J]. Materials Today, 2016, 19: 349−362.

[10] MIRACLE D B, SENKOV O N. A critical review of high entropy alloys and related concepts [J]. Acta Materialia, 2017, 122: 448−511.

[11] PARK J M, MOON J, BAE J W, JANG M J, PARK J, LEE S, KIM H S. Strain rate effects of dynamic compressive deformation on mechanical properties and microstructure of CoCrFeMnNi high-entropy alloy [J]. Materials Science and Engineering A, 2018, 719: 155−163.

[12] RATURI A, BISWAS K, GURAO N P. A mechanistic perspective on the kinetics of plastic deformation in FCC high entropy alloys: Effect of strain, strain rate and temperature [J]. Scripta Materialia, 2021, 197: 113809.

[13] ZHAO Y J, QIAO J W, MA S G, GAO M C, YANG H J, CHEN M W, ZHANG Y. A hexagonal close-packed high-entropy alloy: The effect of entropy [J]. Materials & Design, 2016, 96: 10−15.

[14] SOLER R, EVIRGEN A, YAO M, KIRCHLECHNER C, STEIN F, FEUERBACHER M, RAABE D, DEHM G. Microstructural and mechanical characterization of an equiatomic YGdTbDyHo high entropy alloy with hexagonal close-packed structure [J]. Acta Materialia, 2018, 156: 86−96.

[15] ROGAL L, CZERWINSKI F, JOCHYM P T, LITYNSKA-DOBRZYNSKA L. Microstructure and mechanical properties of the novel Hf25Sc25Ti25Zr25 equiatomic alloy with hexagonal solid solutions [J]. Materials & Design, 2016, 92: 8−17.

[16] ZHANG T W, MA S G, ZHAO D, WU Y C, ZHANG Y, WANG Z H, QIAO J W. Simultaneous enhancement of strength and ductility in a NiCoCrFe high-entropy alloy upon dynamic tension: Micromechanism and constitutive modeling [J]. International Journal of Plasticity, 2020, 124: 226−246.

[17] JIANG Wei, GAO Xu-zhou, GUO Ya-zhou, CHEN Xiang, ZHAO Yong-hao. Dynamic impact behavior and deformation mechanisms of Cr26Mn20Fe20Co20Ni14 high-entropy alloy [J]. Materials Science and Engineering A, 2021, 821: 141858.

[18] ARAB A, GUO Yan-song, SKTANI Z D I, CHEN Peng-wan. Effect of strain rate and temperature on deformation and recrystallization behaviour of BCC structure AlCoCrFeNi high entropy alloy [J]. Intermetallics, 2022, 147: 107601.

[19] TANG Wei-qi, ZHANG Kun, CHEN Tian-yu, WANG Qiu, WEI Bing-chen. Microstructural evolution and energetic characteristics of$TiZrHfTa_{0.7}W_{0.3}$ high-entropy alloy under high strain rates and its application in high-velocity penetration [J]. Journal of Materials Science & Technology, 2023, 132: 144−153.

[20] HE Feng, WANG Zhi-jun, CHENG Peng, WANG Qiang, LI Jun-jie, DANG Ying-ying, WANG Jin-cheng, LIU C T. Designing eutectic high entropy alloys of CoCrFeNiNb_x [J]. Journal of Alloys and Compounds, 2016, 656: 284−289.

[21] HE Feng, WANG Zhi-jun, NIU Si-zhe, WU Qing-feng, LI Jun-jie, WANG Jin-cheng, LIU C T, DANG Ying-ying. Strengthening the CoCrFeNi$Nb_{0.25}$ high entropy alloy by FCC precipitate [J]. Journal of Alloys and Compounds, 2016, 667: 53−57.

[22] HE Feng, WANG Zhi-jun, SHANG Xu-liang, LENG Chao, LI Jun-jie, WANG Jin-cheng. Stability of lamellar structures in CoCrFeNiNb_x eutectic high entropy alloys at elevated temperatures [J]. Materials & Design, 2016, 104: 259−264.

[23] CHANDA B, DAS J. Evolution of microstructure homogeneity and mechanical properties in nano-/ultrafine eutectic CoCrFeNiNb_x ($0.45\leq x\leq 0.65$) high entropy alloy ingots and cast rods [J]. Journal of Alloys and Compounds, 2022, 901: 163610.

[24] MAITY T, PRASHANTH K G, BALCI O, KIM J T, SCHOBERL T, WANG Z, ECKERT J. Influence of severe straining and strain rate on the evolution of dislocation structures during micro-/nanoindentation in high entropy lamellar eutectics [J]. International Journal of Plasticity, 2018, 109: 121−136.

[25] MIAO Ying-gang, LI Yu-long, LIU Hong-yuan, DENG Qiong, SHEN Lu-ming, MAI Yiu-wing, GUO Ya-zhou, SUO Tao, HU Hai-tao, XIE Fa-qin, ZHAO Long, MAO Yong-jian, QI Wei. Determination of dynamic elastic modulus of

polymeric materials using vertical split Hopkinson pressure bar [J]. International Journal of Mechanical Sciences, 2016, 108/109: 188−196.
[26] OUYANG Si-hui, LIU Bin, LIU Yong, ZAN Xiang, LIANG Xiao-peng, LI Zheng. Dynamic tensile behavior of PM Ti−47Al−2Nb−2Cr−0.2W intermetallics at elevated temperatures [J]. Transactions of Nonferrous Metals Society of China, 2019, 29: 1252−1262.
[27] ZHONG Xian-zhe, ZHANG Qing-ming, XIE Jing, WU Ming-ze, JIANG Fu-qing, YAN Yong-ming, WANG Zhi-wei. Mechanical properties and microstructure of the $Al_{0.3}CoCrFeNiTi_{0.3}$ high entropy alloy under dynamic compression [J]. Materials Science and Engineering A, 2021, 812: 141147.
[28] ZHANG Lei-feng, SONG Ren-bo, ZHAO Chao, YANG Fu-qiang. Work hardening behavior involving the substructural evolution of an austenite–ferrite Fe−Mn−Al−C steel [J]. Materials Science and Engineering A, 2015, 640: 225−234.
[29] YANG Fu-qiang, SONG Ren-bo, LI Ya-ping, SUN Ting, WANG Kai-kun. Tensile deformation of low density duplex Fe−Mn−Al−C steel [J]. Materials & Design, 2015, 76: 32−39.
[30] LUO W, KIRCHLECHNER C, ZAVASNIK J, LU W, DEHM G, STEIN F. Crystal structure and composition dependence of mechanical properties of single-crystalline $NbCo_2$ Laves phase [J]. Acta Materialia, 2020, 184: 151−163.
[31] XUE Yun-long, TAKATA N, LI Hong-mei, KOBASHI M, YUAN Liang, Critical resolved shear stress of activated slips measured by micropillar compression tests for single-crystals of Cr-based Laves phases [J]. Materials Science and Engineering A, 2021, 806: 140861.
[32] FREUND M, ANDRE D, ZEHNDER C, REMPEL H, GERBER D, ZUBAIR M, HAUT S S, GIBSON J, KERZEL S. Plastic deformation of the $CaMg_2$ C14-Laves phase from 50−250 °C [J]. Materialia, 2021, 20: 101237.
[33] ZEHNDER C, CZERWINSHI K, MOLODOV K D, HAUT S S, GIBSON J, KERZEL S. Plastic deformation of single crystalline C14 Mg_2Ca Laves phase at room temperature [J]. Materials Science and Engineering A, 2019, 759: 754−761.
[34] TAKATA N, ARMAKI H G, TERADA Y, TAKEYAMA M, KUMAR K S. Plastic deformation of the C14 Laves phase $(Fe,Ni)_2Nb$ [J]. Scripta Materialia, 2013, 68: 615−618.
[35] SHABANI A, TOROGHINEJAD M R. Evaluation of microstructure and texture formation during annealing of cold-rolled FeCrCuMnNi multiphase high-entropy alloy [J]. Transactions of Nonferrous Metals Society of China, 2020, 30: 499−462.
[36] DU Hui, CAI Jia-hong, WANG Ya-song, YAO Jun-qing, CHEN Qiang, CUI Yu, LIU Xin-wang. Effect of partial recrystallization on microstructure and tensile properties of NiFeCoCrMn high-entropy alloy [J]. Transactions of Nonferrous Metals Society of China, 2022, 32: 947−956.
[37] WU Chang-jun, ZHOU Chen, ZENG Jiao-feng, LIU Ya, TU Hao, SU Xu-ping. Effects of annealing at 800 and 1000 °C on phase precipitates and hardness of $Al_7Cr_{20}Fe_xNi_{73-x}$ alloys [J]. Transactions of Nonferrous Metals Society of China, 2021, 31: 734−743.
[38] WANG Jun, LI Hong-chao, YANG Hao-xue, ZHANG Yu, WANG W Y, LI Jin-shan. Hot deformation and subsequent annealing on the microstructure and hardness of an $Al_{0.3}CoCrFeNi$ high-entropy Alloy [J]. Acta Metallurgica Sinica−English Letters, 2021, 34(11): 1527−1536.
[39] LI Dong-yue, GAO M C, HAWK J A, ZHANG Yong. Annealing effect for the $Al_{0.3}CoCrFeNi$ high-entropy alloy fibers [J]. Journal of Alloys and Compounds, 2019, 779: 23−29.

应变速率对 HCP/FCC 双相 $CoCrFeNiNb_{0.5}$ 高熵合金力学性能的影响

马自豪[1]，侯 兵[1]，秦冬阳[1]，李玉龙[2]

1. 西北工业大学 航空学院，西安 710072；
2. 西北工业大学 民航学院，西安 710072

摘 要：利用分离式霍普金斯压杆、扫描电子显微镜和透射电子显微镜研究应变速率对铸态 $CoCrFeNiNb_{0.5}$ 高熵合金力学行为的影响。$CoCrFeNiNb_{0.5}$ 高熵合金由先共析密排六方(HCP)相和共析组织构成，合金的共析结构为片层状的 HCP 相和片层状的面心立方(FCC)相。当应变率从 1×10^{-4} s^{-1} 增加至 6×10^{3} s^{-1} 时，合金的屈服强度不会显著增加；然而，合金的破坏应变剧烈降低。片层状 HCP 相的准静态塑性变形机理为缠结状位错的增殖，而其动态塑性变形机理转变为剪切。片层状 HCP 相的剪切变形能够导致 $CoCrFeNiNb_{0.5}$ 高熵合金在低压缩应变(ε=0.1)下形成微裂纹。由于片层状 HCP 相中微裂纹的数量随着动态压缩应变的提高而增加，微裂纹的扩展引发材料的雪崩式断裂。因此，铸造态 $CoCrFeNiNb_{0.5}$ 高熵合金表现出显著的应变速率诱发脆性特性。

关键词：高熵合金；共析结构；高应变速率；剪切；韧−脆转变

(Edited by Bing YANG)